DEVELOPMENT OF
MICRO-CAVITY

Ho Yew Hung Derek

An academic exercise presented in partial fulfilment for the
degree of Bachelor of Science with Honours in Physics.

Supervisor: Asst. Prof. BARRETT, Murray Douglas

Department of Physics

National University of Singapore

2008/2009

Acknowledgements

Everyone in the Micro Traps group has helped me in one way or another. I am grateful to them all.

I especially thank my supervisor, Murray, for patiently guiding me throughout this project, and allowing me a glimpse into the world of experimental physics research.

I thank PhD students Arpan, Kyle and Boon Leng for their patience in helping me find my way around in the lab whenever I got lost. I also thank research assistant Aarthi for her help in the early stages of the project.

Derek Ho

30 March 2009

Abstract

We set out to fabricate a microcavity in-house, using a method devised by another group, for the first time in our lab. In particular, we wished to investigate for ourselves how well the method could potentially work for us and also discover any problems with it. Using this method, an optical microcavity was fabricated in-house and characterized. The half-symmetric cavity, of length $135\mu m$ and radius of curvature $175\mu m$, displayed a finesse of 800. Some problems with this method were discovered, but the method still holds promise. This project serves as the preliminary trial run for the making of microcavities using this method in our lab.

Contents

Chapter 1

Introduction

This project is about making and characterizing a microcavity. The typical use of microcavities is to satisfy the requirements of the strong coupling regime in cavity quantum electrodynamics, in which individual quanta play a significant role [1] and the coherent, reversible evolution of an atom-cavity system become observable. This strong coupling regime is of experimental interest for various reasons. Firstly, it allows for fundamental investigations into quantum position measurement [1]. For example, strong coupling facilitates quantum position measurements of atomic CM (center of mass) in real-time, which in turn allows one to investigate the standard quantum limit (SQL) of measuring atomic position [2], [3], [4], [5]. Secondly, and with a more application-based perspective, strongly coupled atom-cavity systems are potential building-blocks in quantum information processing applications. Much work has already been done in this direction. Atom chip devices comprising atom traps and microcavities microfabricated on a chip which allow for single atom detection with high bandwidth have been made by various

groups [6], [7], [8]. Such atom chips are potentially useful as quantum logic gates, which are needed for the construction of a quantum computer [9]. Cavities interacting with atoms in the strong coupling regime may also be used for the purpose of entanglement distribution in a quantum network . Entanglement distribution using cavities has been demonstrated experimentally by various groups [10], [11]. These cavities are also useful for single photon sources [12], which serve as flying qubits for distribution of entanglement over large distances. Cavities have also been used for cooling ([13], [14]) and trapping ([4], [15]) of atoms. All these applications with cavities require the successful trapping and localization of atoms. This may be done only if cavities with the right qualities of high finesse and small modal volume are available. This project is about laying the practical groundwork for the fabrication of such a cavity. In particular, we attempt to explore use of an existing method of creating microcavities of small modal volume and, given the appropriate coatings, extremely high finesse. To this end, we will make a microcavity using medium-grade coatings which will be appropriate for the purpose of characterizing the cavity.

The outline for this thesis is as follows. Chapter 2 outlines the background physics needed to understand this project. Chapter 3 covers the methods used to fabricate the cavity as well as other related information. Chapter 4 reports on the measurements made to characterize the cavity. Chapter 5 concludes the thesis by discussing the results of the measurements and further work which may be done beyond the completion of this project.

Chapter 2

Optical Cavities and Cavity Quantum Electrodynamics

Before going into the details of the project, a brief review of the physics involved in this project is given in this chapter.

2.1 Cavity Basics

Optical cavities, consisting of two mirrors placed a certain distance apart, undergo resonance when light of the correct wavelength (or frequency) and geometry is passed through it. In this section, a review of the physics of optical resonance is given. This is followed by an explanation of the concept of mode-matching and the existence of different modes within a cavity.

2.1.1 Resonance of Cavities

The following review is adapted from [16]. For simplicity, we consider here an optical cavity consisting of two plane-parallel mirrors and an incident plane wave. Although the actual experiment involves using a cavity consisting of one planar and one concave mirror (a half-symmetric cavity) and an incident Gaussian $TEM_{0,0}$ beam, the concepts described here are mostly applicable to the actual experiment. The few modifications which are necessary are given in the next subsection.

The two mirrors M_1 and M_2 in the optical cavity of Fig. (2.1) have reflectivities of r_1 and r_2, transmitivitties t_1 and t_2 and losses a_1 and a_2 respectively. These quantities represent the fraction of the *electric field amplitude* which is reflected, transmitted or lost respectively when an electric field impinges upon $M_{1(2)}$. The losses here include both losses through absorption and scattering .

Since the energy in any electric field is proportional to the square of its amplitude, conservation of energy requires that

$$R_{1(2)} + T_{1(2)} + A_{1(2)} = 1 \tag{2.1}$$

where the uppercase letters have been used to represent the modulus-squares of their corresponding lowercase ones, and are respectively called the reflection, transmission and loss coefficients. They refer to the fraction of the *energy* which is reflected,transmitted or lost.
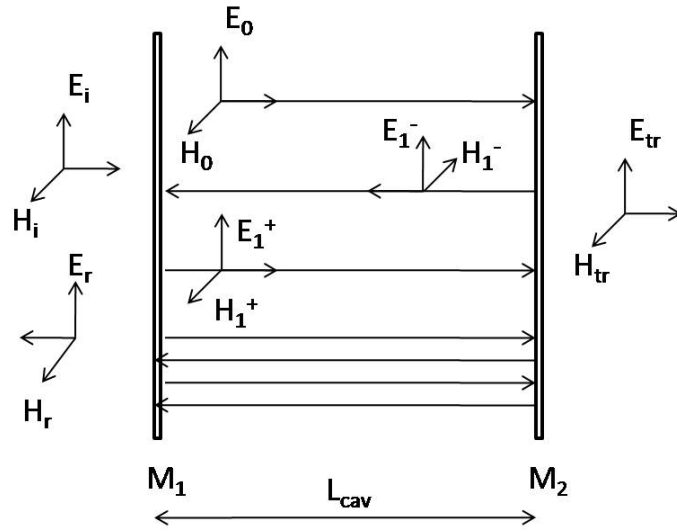
Figure 2.1: **An optical cavity consisting of two plane mirrors.** This image is adapted from [16].

When the laser first enters the cavity of length L_{cav}, an initial electric field of amplitude E_0 appears just to the right of M_1. This wave travels to mirror M_2 and gets reflected to produce a wave travelling towards the left with an electric field given by $r_2 E_0 e^{-ikd}$. This wave is then reflected again at M_1 to produce a wave just to the right of M_1 travelling to the right, described by $r_1 r_2 E_0 e^{-i2kd}$. At this location, there is also a new incident field E_0 introduced into the cavity by the laser, which is exactly one round-trip behind. This process of fields bouncing back and forth while being joined by new ones clearly can go on for any number of times as long as the laser remains switched on. Hence, the total field propagating to the right at the location just to the right of M_1, is simply the sum of these waves, which may be written as an infinite geometric progression as follows.

$$E_T^+ = \sum_0^\infty E_n^+ = E_0 \left[1 + r_1 r_2 e^{-ik2d} + \left(r_1 r_2 e^{-ik2d} \right)^2 + etc \right] = \frac{E_0}{1 - r_1 r_2 e^{-i2\theta}}$$

$$(2.2)$$

where $\theta = kL_{cav}$, is the electrical length of the cavity, which is the phase picked up by the field in travelling the length of the cavity. k simply denotes $\frac{2\pi}{\lambda}$.

The total field travelling toward the left just to the right of M_1 is $r_2 e^{-2i\theta}$ of E_T^+. Hence,

$$E_T^- = \sum E_n^- = r_2 e^{-2i\theta} \cdot E_T^+ = E_0 \left[\frac{r_2 e^{-2i\theta}}{1 - r_1 r_2 e^{-2i\theta}} \right] \qquad (2.3)$$

We wish to find the relationship between the incident field entering the cavity, E_i, and the reflected and transmitted fields, E_r and E_{tr}, respectively. We do this by noting that E_T^+ and E_T^- are related via the following equation, which is simply the intuitive statement that the total field travelling toward the right is the sum of the fields transmitted and reflected by M_1. (the field picks up a phase factor of i when it gets transmitted.)

$$E_T^+ = it_1 E_i + r_1 \sum E_T^- \qquad (2.4)$$

The above result can be combined with the previous two equations to yield the relation between E_0 and E_i as follows.

$$E_0 = it_1 E_i \qquad (2.5)$$

6

The field reflected from the cavity is the sum of the portion of the incident field that gets reflected by M_1 and the total field travelling to the left within the cavity that gets transmitted through M_1.

$$E_r = r_1 E_i + it_1 \sum E_n^-$$
(2.6)

Substitution for E_0 and $\sum E_n^-$ in the above equation using equations (2.5) and (2.3) respectively and some simple algebraic manipulation obtains the ratio of the fields *reflected* from and incident upon the cavity. We are interested in the fraction, T, of the incident power which gets transmitted through the cavity, so we take the modulus-squared of this quantity to obtain

$$T = \frac{(1 - R_1 - A_1)(1 - R_2 - A_2)}{\left(1 - \sqrt{R_1 R_2}\right)^2 + 4\sqrt{R_1 R_2} sin^2\theta}$$

(2.7)

where equation (2.1) has been used to write T only in terms of reflectivities and losses.

One may also obtain the ratio of the fields *transmitted* through and *incident* upon the cavity by noting that the field transmitted is simply given by $it_2 e^{-i\theta} \sum E_n^+$. Again, we are interested in the fraction, R of the incident power reflected from the cavity, so we take the modulus square of this to obtain

$$R = \frac{R_1 + R_2\left(1 - A_1\right)^2 - 2\sqrt{R_1 R_2}\left(1 - A_1\right) + 4\sqrt{R_1 R_2}\left(1 - A_1\right)sin^2\theta}{\left(1 - \sqrt{R_1 R_2}\right)^2 + 4\sqrt{R_1 R_2}sin^2\theta}$$

$$(2.8)$$

Equations (2.7) and (2.8) are very important. They will be needed later for making sense of the experimental measurements of the reflection and transmission of the cavity. Note that when both mirrors have equal reflection coefficients, and zero loss coefficients, and θ is an integer multiple of π, the transmission is unity and the reflection is zero. This situation, in which θ is an integer multiple of π so that the cavity transmission reaches its maximum is known as resonance. M_2 is typically highly reflective, yet we have an amount of power equal to the incident power exiting through it. This observation tells us that the intracavity field during resonance is many times that of the input field. This is an essential feature of resonance. It is responsible for the increased interaction between photons and atoms in a cavity. This will be discussed in the next section.

It can be easily shown by substitution that as the reflection coefficients of the mirrors become more different, T decreases while R increases during resonance. Hence, mismatch of the reflection coefficients reduces our ability to couple light into the cavity. When θ is approximately $\frac{\pi}{2}$, the transmission is essentially zero and the reflection is unity. This situation is known as anti-resonance.

We now analyze the phenomenon of resonance in more detail. As mentioned, resonance occurs when the following condition is fulfilled:

$$\theta = kL_{cav} = q\pi \tag{2.9}$$

where q is any integer number.

Writing Eq. (2.9) in terms of wavelength, frequency and angular frequency, we obtain respectively

$$L_{cav} = \frac{m\lambda}{2} \tag{2.10}$$

$$\nu_m = \frac{c}{2nL_{cav}} \tag{2.11}$$

$$\omega_m = m\frac{\pi c}{nL_{cav}} \tag{2.12}$$

where m is some integer number and $\omega_m(\nu_m)$ refers to the corresponding resonant angular frequency(frequency) of the cavity. n simply refers to the refractive index of the medium of the cavity. For our purposes, this was simply free space so we may treat n as unity in our calculations.

A look at Eq. (2.2) shows that Eq. (2.9) simply describes the situation when all the fields in the summation of Eq. (2.2) are in phase, which means that all the fields exiting the cavity through M_2 will interfere constructively regardless of how many round trips each one has made before exiting. Also, it may be seen from Eq. (2.6) that when Eq. (2.9) is satisfied, the fields exiting the cavity through M_1 have a phase difference of exactly π with the portion of the incident field reflected from M_1, resulting in destructive interference between the two. The latter two statements explain why transmission is maximized and reflection minimized during resonance.

The full-width half maximum, or linewidth, of the cavity, $\Delta\nu_{\frac{1}{2}}$, which is found from Eq. (2.7) through simple algebraic manipulation, is given by

$$\Delta\nu_{\frac{1}{2}} = \frac{c}{2nd}\frac{1-(R_1 R_2)^{\frac{1}{2}}}{\pi(R_1 R_2)^{\frac{1}{4}}} = \frac{\Delta\nu_{FSR}}{F} \tag{2.13}$$

where

$$\Delta\nu_{FSR} = \frac{c}{2nL_{cav}} \tag{2.14}$$

is the free spectral range (also known as axial mode spacing) of the cavity, which is the difference between adjacent resonant frequencies.

and

$$F = \frac{\pi(R_1 R_2)^{\frac{1}{4}}}{1-(R_1 R_2)^{\frac{1}{2}}} = \frac{\Delta\nu_{FSR}}{\Delta\nu_{\frac{1}{2}}} \tag{2.15}$$

is the finesse of the cavity. From the second expression for F, we see that F is a measure of how sharp the resonance is.

The cavity linewidth determines the decay rate of photons in the cavity. This may be seen as follows. For the purpose of this illustration, it is assumed that $R_1 = R_2 \equiv R \simeq 1$, which is usually indeed the case in practice. If at time $t = 0$, a pulse of N photons is created at the center of the cavity and travels towards one of the mirrors, then after time $t = \frac{nL_{cav}}{c}$, the photon number would have decreased to RN. Hence, the following differential equation applies:

$$\frac{\mathrm{d}N}{\mathrm{d}t} = -\frac{\Delta N}{\frac{nL_{cav}}{c}} = -\frac{c(1-R)}{nL_{cav}}N \tag{2.16}$$

10

Solving this yields $N = N_0 e^{-\frac{t}{\tau_{cav}}}$, where the photon lifetime τ_{cav} is

$$\tau_{cav} = \frac{nL_{cav}}{c\,(1-R)} \tag{2.17}$$

The cavity photon decay rate κ is then defined simply as $\kappa = \frac{1}{\tau_{cav}}$. Combining this expression with Eq.(2.15) and applying the estimation $R \simeq 1$ yields

$$\kappa = 2\pi\Delta\nu_{\frac{1}{2}} = \Delta\omega \tag{2.18}$$

Hence, the linewidth of the cavity $\Delta\omega$, is equal to the decay rate of the cavity-the narrower the cavity's linewidth, the longer photons can stay confined within its walls. It is also obvious from Eq. (2.15) that the decay rate of a cavity is less for a higher finesse cavity. The quality factor, Q, of a cavity also serves a similar purpose as the finesse, and is defined by

$$Q = \frac{\nu_0}{\Delta\nu_{\frac{1}{2}}} \tag{2.19}$$

where ν_0 is the particular resonant frequency of the cavity in question.

In summary, this section has introduced the important characteristics of cavity resonance. The transmission and reflection of the cavity are quantified by equations (2.7) and (2.8). The quality of the cavity is quantified by the linewidth, and hence the finesse and Q factor.

11

2.1.2 Gaussian Modes and Mode-Matching

The previous scenario assumed a planar cavity with an incident plane wave. In practice, Gaussian modes are usually used, with either one or both cavity mirrors being curved. In this case, resonance requires not only that we get the cavity length right, but also that we match the geometry of the laser beam with that of the cavity mirrors. This practical matter is known as **mode-matching** of a beam to the cavity.

It is sufficient for our purposes to consider only transverse electromagnetic (TEM) modes. These are one class of solutions to the Maxwell equations in free space and they essentially tell us the shape of our lasers. The general electric fields for $\text{TEM}_{m,p}$ modes are given by

$$
\begin{aligned}
\frac{E\left(x, y, z\right)}{E_{m,p}} \;=\;\; & H_m\left[\frac{2^{\frac{1}{2}}x}{w\left(z\right)}\right] H_p\left[\frac{2^{\frac{1}{2}}y}{w\left(z\right)}\right] \\[2mm]
& \times \frac{w_0}{w_z}\exp\left[-\frac{x^2 + y^2}{w^2\left(z\right)}\right] \\[2mm]
& \times \exp\left\{-i\left[kz - (1 + m + p)\tan^{-1}\left(\frac{z}{z_0}\right)\right]\right\} \\[2mm]
& \times \exp\left[-i\frac{kr^2}{2R\left(z\right)}\right]
\end{aligned}
\tag{2.20}
$$

where H refer to Hermite polynomials, and

$$w^2(z) = w_0^2 \left[1 + \left(\frac{z}{z_0} \right)^2 \right] \tag{2.21}$$

$$R(z) = z \left[1 + \left(\frac{z_0}{z} \right)^2 \right] \tag{2.22}$$

$$z_0 = \frac{\pi w_0^2}{\lambda_0} \tag{2.23}$$

$w(z)$ is the spot size of the beam. w_0 is the minimum value of the spot size and is referred to as the beam waist. It may be seen here that the position of the beam waist defines the origin $z = 0$. $R(z)$ is the radius of curvature of the beam. For a TEM$_{0,0}$ mode, these quantities are easily visualized in Fig.(2.2). z_0 is the Rayleigh length of the beam.
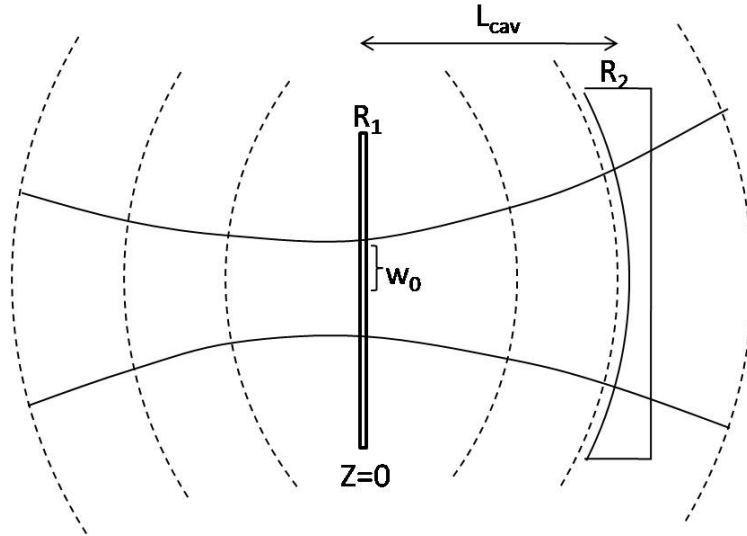

Figure 2.2: **Propagation of a TEM$_{0,0}$ mode through a half-symmetric cavity.**The curved dotted lines represent the wavefronts of the beam. In order for resonance to occur, the radius of curvature of the beam at the mirrors must match that of the mirrors.Diagram is adapted from [16].

In order for a beam to resonate within the half-symmetric cavity used for this project, the wavefronts of the beam at the mirrors must match the mirror surfaces, just as the wavefronts of the plane wave matched the flat mirror surfaces in the previous section. The $\text{TEM}_{0,0}$ beam changes its radius of curvature as it propagates through space, as seen from Eq. (2.22). The modes are matched if the beam reaches the mirror with a radius of curvature equal to that of the mirror. In the case of our half-symmetric cavity, this means that the radius of curvature must be infinite at the plane mirror. From Eq.(2.21), this is equivalent to saying that the beam waist must occur at the plane mirror. From Eqs.(2.22) and (2.23), it may be seen that in order for the beam curvature to match that of the curved mirror for a given cavity length, the correct size of beam waist w_0 must be used. Usually, and as is the case in this project, a lens is placed at an appropriate distance before the cavity. A collimated beam is then passed through the lens so that the correct size beam waist occurs at the planar mirror. In order to know which focal length of lens is appropriate, we make use of the following formula

$$w_{out} = \frac{\lambda f}{\pi w_{in}} \tag{2.24}$$

This formula, together with Eqs. (2.22),(2.21) and (2.23), are used for mode-matching. The $\text{TEM}_{0,0}$ mode described above has just the right geometry to resonate in the half-symmetric cavity. It is thus referred to as the privileged mode of the cavity. Misalignments of the beam can cause other unwanted modes to start resonating. This issue will be discussed in the next chapter.

In this project, we deal with curvatures on the order of $100 - 200 \mu m$. Hence,

we need very small values for the beam waist, on the order of several microns. Such small waists cannot be measured straightforwardly using the typical commercial beam profilers on the market. It is necessary to use a high-resolution imaging system followed by a curve-fit to the pixel data in Matlab in order to measure the beam waist. This is discussed in detail in Chapter 4.

2.1.3   Axial and Transverse Mode Spacing

Just as Eq. (2.11) tells us the resonant frequencies of the planar cavity with plane waves, it is possible to obtain a formula for the resonant frequencies of the Gaussian modes in our half-symmetric cavity.

The phase shift experienced by a $\text{TEM}_{m,p}$ mode in propagating from $z = 0$ to $z = d$ is given by

$$\phi(0 \rightarrow d) = kd - (1 + m + p)\tan^{-1}\left(\frac{d}{z_0}\right) \qquad (2.25)$$

Resonance occurs when $\phi = q\pi$, for the same reasons mentioned previously. For the half-symmetric cavity of length d in Fig. (2.2), Eq. (2.22) provides a relation between z_0 and R_2:

$$z_0 = (dR_2)^{\frac{1}{2}}\left(1 - \frac{d}{R_2}\right)^{\frac{1}{2}} \qquad (2.26)$$

Substituting this into $\phi = q\pi$ yields an expression for the resonant frequencies of the Gaussian modes in the cavity:

$$\nu_{m,p,q} = \frac{c}{2nd} \left[q + \frac{1+m+p}{\pi} \cos^{-1}\left(1 - \frac{d}{R_2}\right)^{\frac{1}{2}} \right] \qquad (2.27)$$

Modes for which $m = p = 0$ are known as axial modes. We can see from this equation that the the axial mode spacing, which is the difference between modes of adjacent q values and $m = p = 0$, is equivalent to the free spectral range given in Eq.(2.14). Modes which do *not* have zero values for m and p are referred to as transverse modes. From Eq. (2.27), it may be seen that for a particular q value, adjacent modes are separated in frequency space by the transverse mode spacing, defined by

$$\frac{1}{\pi} \cos^{-1}\left(1 - \frac{d}{R_2}\right)^{\frac{1}{2}} \qquad (2.28)$$

This raises the practical issue of mode degeneracy within a cavity. It is clear from the above equation that modes of different m and p will overlap in frequency space.

Another issue is that the cavity can resonate in modes other than the privileged one when the input beam (of constant frequency) is slightly misaligned. Our half-symmetric cavity has a geometry which coincides with a particular axial mode depending on the cavity length, making this mode the privileged one. However, a misalignment of the beam with respect to the optic axis of the cavity can result in the cavity resonating in the neighbouring transverse modes in addition to the privileged mode. This is undesirable as it will eventually result in reduced coupling between an atom and the privileged mode when the cavity is used for cavity quantum electrodynamics experiments (see next section). Considerable effort is thus required in practice to

16

align the beam so that the cavity resonates only in the privileged mode.

2.2 Brief Review of Cavity Quantum Electro-dynamics

A brief review of the relevant cavity quantum electrodynamics (CQED) is given here, based on the review paper in [1] and [17]. Fig. 2.3 shows a model system in which a two state atom is located in an optical cavity consisting of two spherical mirrors.
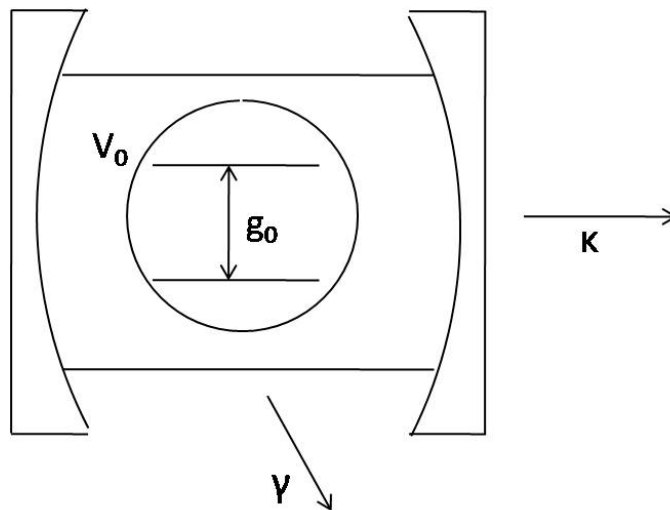

Figure 2.3: **Diagrammatic representation of atom-photon interaction within a cavity.** As seen from the diagram, the atom can spontaneously emit a photon sideways, represented by γ, or the photon can pass through the cavity walls, as represented by κ. The region enclosed by the horizontal lines represents the cavity mode volume, V_0. This diagram is adpated from [17].

The Hamiltonian for the atom-cavity system is given by

$$\hat{H}_s = \frac{\hbar\omega_A}{2}\hat{\sigma}^z + \hbar\omega_C\hat{a}^\dagger\hat{a} + i\hbar\left[g(\mathbf{r})\hat{a}^\dagger\hat{\sigma}^- - g^*(\mathbf{r})\hat{a}\hat{\sigma}^+\right] \tag{2.29}$$

The operator $\hat{a}$ and $\hat{a}^\dagger$ are the annihilation and creation operators for the single-mode of the resonator under consideration respectively. σ^z and $\hat{\sigma}^\pm$ are the Pauli operators for the atomic inversion, raising, and lowering, respectively. ω_A and ω_C are the atomic and cavity resonance frequencies. $g(\mathbf{r})$ is the coherent coupling rate between the atom at position $\mathbf{r}$, which we may take for our purposes to be given by

$$\begin{aligned}g(\mathbf{r}) &= \left(\frac{\mu^2\omega_C}{2\hbar\epsilon_0 V_{m,n}}\right)^{\frac{1}{2}} U(\mathbf{r}) \tag{2.30}\\ &\equiv g_0\, U(\mathbf{r})\end{aligned}$$

μ is the transition dipole moment for the two-state atom. $V_{m,n}$ is the cavity mode volume, given by

$$\begin{aligned}V_{m,n} &= \frac{\pi w_0^2}{2}L_{cav}\left(m!n!2^{n+m}\right) \tag{2.31}\\ &= \frac{\pi w_0^2}{2}L_{cav} \qquad (\text{for the TEM}_{0,0}\text{mode})\end{aligned}$$

For our purposes, we may make the simplifying approximation in Eq. (2.31) that $g(\mathbf{r})$ is given by g_0. This is because most experiments make use of a trap, typically a dipole force trap, to restrict the atom's position in the cavity to regions where $U(\mathbf{r}) \simeq 1$.

There are two loss mechanisms for loss of photons from the cavity. Firstly, photons may get transmitted through the cavity walls at a rate quantified by the cavity decay rate κ, as explained in the previous section and defined in Eq. (2.18). Secondly, photons may be lost through a combination of other mechanisms, at a rate quantified by the non-resonant decay rate γ. The loss mechanisms involved in this rate are as follows. Photons may be radiated in a direction that misses the walls. Alternatively, the atom may decay to another level other than the ground state in the two-level atom approximation. Excited atoms may also fall back to the ground state through scattering to other states and decaying without any photon emission.

Here we may take $\gamma \equiv \frac{\gamma_{\parallel}}{2}$, where

$$\gamma_{\parallel} = A_{21} \left(1 - \frac{\Delta \Omega}{4\pi} \right) \tag{2.32}$$

where A_{21} is the Einstein A coefficient for spontaneous emission and $\Delta \Omega$ the solid angle subtended by the cavity mode.

A derivation of the condition for strong coupling is beyond the scope of this thesis, so the condition shall be simply stated. Strong coupling occurs when

$$g_0 \gg (\gamma, \kappa) \tag{2.33}$$

which means that the coherent coupling rate must be larger than both the non-resonant decay rate and cavity decay rate. It is worth noting here that in order for g_0 to be larger than κ, we need a high finesse cavity, as seen from Eq. (2.15). Also, we require a small mode volume. This is why we require

microcavities with high finesse in order to achieve strong coupling. Another note worth making here is that from Eq. (2.32), we need not have a very small cavity (ie. very small L_{cav}) if we can compensate for this by using a very small beam waist w_0.

In the regime of strong-coupling, the energy levels of the atom-photon system undergo splitting. This splitting effect is needed for the various experiments done in the strong coupling regime. For example, the trapping potential in cavity trapping occurs due to this energy splitting [15]. Single atom detection in cavities is also made possible because of the energy splitting- the energy split leads to a splitting of a single peak into two in the transmission vs. frequency spectrum when an atom passes through the cavity [18].

The physics behind this energy splitting is essentially described in the **Jaynes-Cummings Model**. A simplified review of this model, adapted from that given in [17], is given here.

We consider a two-level atom of angular frequency ω within a resonant cavity. The atom-photon states, Ψ in the absence of atom-cavity interaction (ie. in the absence of strong coupling), are labelled by the state of the atom ψ and the number of photons in the cavity n, so

$$\Psi = \mid \psi; n \, \rangle \tag{2.34}$$

The ground state occurs when the atom is in the ground state with no photons in the cavity: $\Psi_0 = \mid g; 0 \, \rangle$. The ground state is non-degenerate with an energy of $\frac{1}{2}\hbar\omega$ due to the zero-point energy of the vacuum field in the cavity. The excited states are all doubly degenrate. For example, the first excited state

with energy $\frac{3}{2}\hbar\omega$ corresponds to two states- $\mid e;0 \rangle$ and $\mid g;1 \rangle$, corresponding to the atom being in the excited state with no photons present and the atom being in the ground state with a single photon present respectively.

In the presence of strong coupling, the electric-dipole interaction between the atom and photon mixes the degenerate states and lifts their degeneracy. Hence, the first excited state becomes a doublet with energies given by

$$E_1^\pm = \left(\frac{3}{2}\right)\hbar\omega \pm \hbar g_0 \tag{2.35}$$

with corresponding wavefunctions

$$\Psi_1^\pm = \frac{1}{\sqrt{2}}\left(\mid g;1 \rangle \mp \mid e;0 \rangle\right) \tag{2.36}$$

The other states are also split similarly so that

$$
\begin{aligned}
E_n^\pm &= \left(n+\frac{1}{2}\right)\hbar\omega \pm \sqrt{n}\hbar g_0 \\
\Psi_n^\pm &= \frac{1}{\sqrt{2}}\left(\mid g;n \rangle \mp \mid e;n-1 \rangle\right) \\
\Delta E_n &= 2\sqrt{n}\hbar g_0
\end{aligned}
\tag{2.37}
$$

where the last equation is the energy splitting for the nth level. The mixed atom-photon states are known as dressed states and the ladder of doublets, which starts from $n = 1$, is the Jaynes-Cummings ladder. As mentioned earlir, this energy splitting is responsible for many of the novel effects seen in the strong coupling regime.

Chapter 3

Cavity Fabrication Methods and Considerations

3.1 Considerations for Design of Micro-Cavity

In order to decide on the design of the cavity, we have to consider issues such as the alignment stability of the cavity as well as the overlapping of the cavity modes.

3.1.1 Alignment Stability

In order for the cavity to resonate in single-mode, we require that the optic axis defined by the two mirros pass through or be near the center of each mirror. In the worst case scenario, misalignment can result in the optic axis leaving the cavity altogether, resulting in the absence of any resonance.

Misalignments may take the form of translational or rotational misalignments, in which the mirrors are rotated at some angle with respect to each other so that the optic axis misses the centers of the mirrors. To obtain a sense of the magnitude of translational and rotational misalignment which a micro-cavity can tolerate, we consider two concave mirrors of curvature R and calculate the amount by which the optic axis deviates from the centers of the two mirrors for small amounts of translational and rotational misalignment using typical cavity parameters. To facilitate easy calculation, we may consider these two misalignments one at a time separately.

We consider first the case of translational misalignment, as shown in Fig. (3.1).
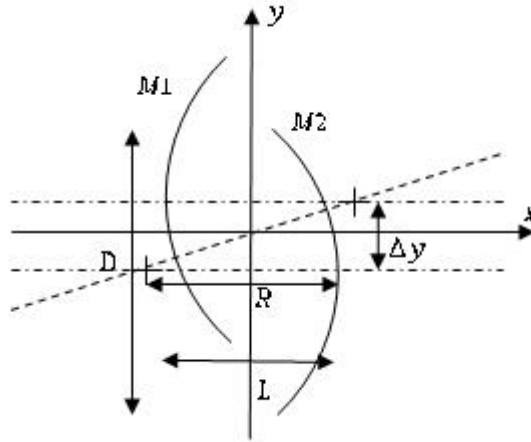

Figure 3.1: **Vertical misalignment.** Two mirrors which were originally in perfect alignment with their centers on the x axis have been displaced vertically. M1 has been displaced upwards by $\frac{\Delta y}{2}$ while M2 has been displaced downwards by an equal amount.

The cavity length is denoted by L. Assuming that the mirrors M1 and M2 started out with their centers positioned symetrically at $\left(\pm\frac{L}{2}, 0\right)$, with no tilting between them, the figure shows the mirrors after they have been respectively displaced by $\frac{\Delta y}{2}$ below and above the x-axis respectively, giving a net displacement of Δy between them. The centers of the mirror curvatures are denoted by crosses. The optic axis is defined as the line joining these centers of curvature. We wish to find the difference in position between the center of mirror M2 and the point where the optic axis intersects with M2. We wish to make sure that this intersection point is still reasonably near the center of the mirror for small translational misalignments of the mirrors. On the cartesian axes in Fig. (3.1), the equations for the optic axis and mirror M2 are given respectively by

$$y = \frac{\Delta y}{2\left(R - \frac{L}{2}\right)}x \tag{3.1}$$

$$R^2 = \left(y + \frac{\Delta y}{2}\right)^2 + \left(x + \left(R - \frac{L}{2}\right)\right)^2 \tag{3.2}$$

For a typical misalignment of say $\Delta y = 10\mu m$ (the uncertainty of readings on our translation stage's micrometers is $10\mu m$), and typical curvature and cavity length $R = 150\mu m$ and $L = 137.5\mu m$, we find that the intersection point between optic axis and mirror M2 occurs at $(68.5\mu m, 4.21\mu m)$. The distance from this intersection to the center of the mirror M2 at $(\frac{L}{2}, -\frac{\Delta y}{2})$ is found to be $9.21\mu m$, which is still within acceptable range, as the cross-sectional diameter of the mirrors, labelled D, (ie. the radius of the circle seen under the microscope when looking at an exposed bubble) are on the order of $200 - 250\mu m$ for mirrors of $R = 150\mu m$, since the bubbles are polished to

24

slightly beneath the half-way mark. A misalignment of $20\mu m$ results in the optic axis intersecting $M2$ at a distance of 64 μm from its center. This is still within the mirror $M2$, but we see that misalignments of more than $20\mu m$ are a cause for concern. This is not really a problem as achieving a translational alignment accuracy to within $10\mu m$ should not be a problem given the spatial resolution of translation stages available on the market today.

We consider next the problem of rotational misalignment. Once again assuming the mirrors started out with no rotational misalignment and their centers positioned at $\left(\pm\frac{L}{2}, 0\right)$, we consider the situation where both mirrors have each been rotated by $\frac{\theta}{2}$, so that they have a net angular misalignment of θ radians. This situation is shown in Fig. (3.2).
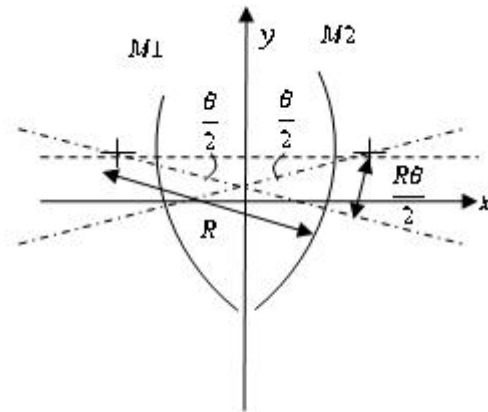

Figure 3.2: **Rotational misalignment.** Two mirrors which were originally in perfect alignment with their centers on the x axis have each been tilted so that their optic axes form an angle of $\frac{\theta}{2}$ with respect to the horizontal axis. This means that the optic axes form an angle of θ with each other.

The deviation of the intersection of the optic axis and mirror M2 is taken as $\frac{R\theta}{2}$. This slightly over-estimates the error- if this quantity is an acceptable value, so too is the actual error. We require the deviation $\frac{R\theta}{2}$ to be much less than $\frac{D}{2}$, which is half the cross-sectional diameter of the mirror, as defined in Fig. (3.1). In order for the deviation to be equal to $\frac{D}{2}$, we require a total angular misalignment of $\theta = 57.3°$. For a more reasonable misalignment of $\theta = 1°$, we obtain a deviation of $\frac{R\theta}{2} = 1.5\mu m$, where we have used the same value for R as before. A misalignment of $1°$ is larger than what we would expect in the real setup. Hence, we may conclude that rotational misalignment is not likely to be a major cause for concern. The greater concern would be the translational misalignment of our mirrors.

In order to make it easier to align the mirrors, we decided upon the half-symmetric cavity design, in which the cavity consists of one plane mirror and one curved micro-mirror. This means that we need only worry about the rotational misalignment of the mirrors, since the plane mirror does not 'see' the translational misalignment described previously due to its symmetry along the planar direction.

3.1.2   Important Cavity Parameters

Here, we make use of the formulae outlined in Chapter 2 to calculate the expected values of some important cavity parameters.

For an estimated cavity length of $135\mu m$ and radius of curvature $175\mu m$, the free spectral range, given by Eq. (2.14), is 1.11 THz, while the transverse mode spacing is 0.341 of a free spectral range, or 0.379 THz, as given by Eq.

(2.28).

The linewidth of the cavity,$\Delta\nu_{\frac{1}{2}}$, is given by Eq.(2.13), where F is the finesse of the cavity. For the purposes of this project, we did not intend on using the best mirror coatings on the market, which can give F on the order of 10^5 or better. This is because these coatings can only be done overseas and would take possibly several months. This was unacceptably long a time to wait for a 2 semester project. Moreover, we do not need such high reflection coefficients for a first iteration of making cavities using this technique- this project is after all about making these cavities and finding out how well they work and what issues might be associated with them. Hence, we decided to go for lower quality coatings which give an expected finesse of about 1000. These coatings could be done locally and had a turnaround time of one week. A finesse of 1000 gives us a linewidth of 1.11GHz.

It is useful to calculate these parameters in order to have an idea of the spacing between modes. When the cavity first begins to resonate during the alignment process, we typically see many modes in our scope. These figures above help us to make sense of what we are seeing. For example, they give us an idea of how many transverse modes we should expect to see between axial modes.

We now calculate the g factor for such a cavity and see if it fulfills the strong coupling requirement for a rubidium atom, which is a typical atom used in such experiments. For $780nm$ light, the spontaneous decay rate is $4 \times 10^7 s^{-1}$. We may take this as our γ parameter for our purposes. We then make use of the following formulae from [6], which are more convenient forms of Eqs. (2.31) and (2.15).

$$g = \sqrt{\frac{3\lambda^2}{\pi^2 w_1^2} \frac{c\gamma}{L_{cav}}} \qquad (3.3)$$

$$\kappa \simeq \frac{\pi}{F} \frac{c}{2L_{cav}} \qquad (3.4)$$

We assume a typical beam waist of about $3\mu m$, which we can bring about in the lab using aspheric lenses. We assume a finesse of 1000 as before. We then obtain $g = 1.35 \times 10^9 s^{-1}$, and $\kappa = 3.49 \times 10^9 s^{-1}$. Hence, our cavity was not expected to fulfill the strong coupling criterion. However, it is important to note that if we were to use high quality coatings giving F of 10^5, then $\kappa = 3.49 \times 10^7$. This satisfies the strong coupling regime requirement. How well a cavity satisfies the criterion is quantified by $\frac{g^2}{\kappa\gamma}$. For our current cavity, this works out to 13. For a cavity with $F = 10^5$, this works out to 1300. This means that this cavity design is potentially able to bring us well into the strong coupling regime.

3.2   Making of Curved Micro-Mirror Substrate

The curved micro-mirror substrate was fabricated based on the procedure devised by Cui. et. al [19] shown in Fig.(3.3). Borosilicate glass tubes were melted in a nitrogen atmosphere at 1100K. Gas bubbles are trapped inside the glass during the melting process. Upon cooling and hardening, these bubbles are formed inside the solid glass with an expected high degree of sphericity due to surface tension.
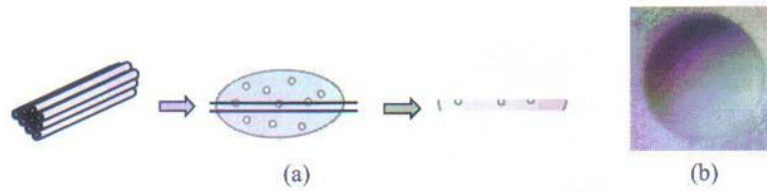
Fig. 2. (a) Melting borosilicate glass tubes to form nitrogen gas-bubbles in the glass and polishing the glass bulk into a $150\,\mu$m-thick slide. (b) 40X pictures of a dimple. Diameter of the dimple $= 200\,\mu$m.

Figure 3.3: **The procedure used for developing bubbles.** The glass tubes are melted and upon cooling capture bubbles. These bubbles can be exposed and coated to serve as micro-mirrors.This diagram is taken from [19].

A bubble of suitable size is selected and the glass is ground down on a polishing wheel to expose part of the selected bubble, as shown under a 5X microscope objective in Fig.(3.4). This is a time-consuming process as it requires using an optical microscope to find a bubble on each glass substrate which is both of a suitable size and also does not have any bubbles further beneath, as the presence of such bubbles would cause scattering of light as it passes through the glass.

The radius of curvature of the micro-mirror is given by the radius of the bubble used to make it. Hence, the radius of curvature is obtained during this polishing process as follows. When viewed under the microscope, the bubble appears as a circle as seen in Fig.(3.4). As the bubble is polished further down, the size of this circle increases to a maximum, corresponding to the exactly half the bubble being polished away, and then decreases as the polishing proceeds beyond the halfway point. The diameter of the circle is
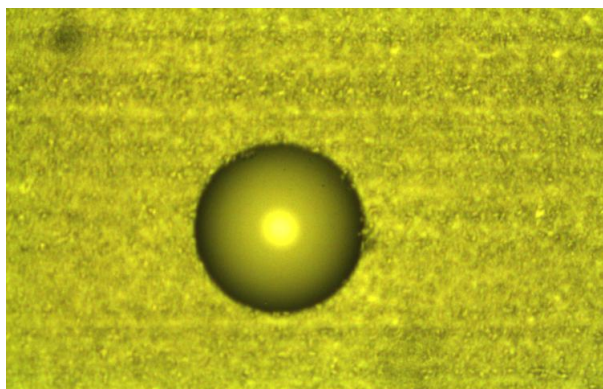
29

Figure 3.4: **A Typical Exposed Bubble seen under 5X.** This is a typical bubble after exposure through grinding seen under 5X microscope objective. As expected, the bubble shows a circular cross-section. The diameter of the circular hole shown above is $260\mu m$.

measured at intervals between polishing. The radius of curvature is obtained by taking half of the maximum diameter measured. This method is accurate to a good degree because the cross-sectional diameter of a sphere varies very slowly near the middle of the sphere. This will be discussed more in the next section.

The top surface, with the open bubble, is finished on the polishing wheel with a diamond disc with nickel-plated diamonds in a raised dot matrix pattern of $30\mu m$ grit size. The bottom surface is polished using a polishing cloth with $0.05\mu m$ colloidal silica suspension on it, giving an optical-quality finish. Cui et. al. [19] reported that they achieved nanometer roughness on the bubbles' interior using this method. Also, they report a high degree of sphericity- at the bottom of a dimple, in a circle of $15\mu m$ diameter, the deviation from perfect sphericity was found to be less than $10nm$ as measured with a Wyko interferometer [19].

After this process, we found considerable contamination inside the open bubble. After considerable trial and error, it was discovered that cleaning the substrate ultra-sonically in Acetone, followed by distilled water, each time for 5 minutes at 25 kHz, appeared to remove the contaminants, without causing any observable damage to the dimple. The bubbles' interior viewed under a $10X$ microscope objective looked fairly smooth, as shown in Fig.(3.5). However, we noticed some possible pits at the base of the dimple.
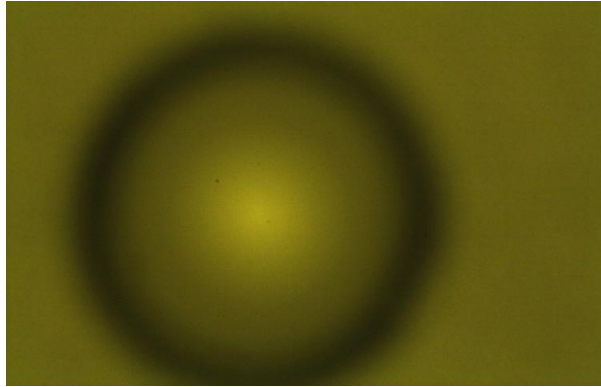

Figure 3.5: **Interior of a bubble before coating under 10X.** This is an example of what the base of a bubble seen through a 10X microscope objective looks like. Note that some blemishes are discernible if one looks closely.

Twelve substrates were created in this fashion and sent to a commercial company for optical coating (Opto-Precision Pte Ltd, Singapore). The instruction to the company was to coat the top side of the glass substrate (with the exposed bubble) with a high-reflectivity coating possessing reflection coefficients $99.25 - 99.50\%$ and transmission coefficients $0.25 - 0.5\%$ at $780nm$. Flat pieces of borosilicate glass with the same coatings were also purchased from the company to serve as the flat mirror in our half-symmetric cavity.

Unfortunately, the company did not follow our instructions and the transmission of the coating which they provided turned out to be extremely low, at about 0.01%. This later posed a problem for us in terms of characterizing the transmission of our cavity. The lower side of the glass substrate was coated with an anti-reflective coating of less than 0.5% reflection coefficient at $780nm$.

Upon receiving the coated micro-mirror dimples, we set them up in an imaging system (more on this imaging system in the next chapter) involving a $50X$ microscope objective in order to confirm the radius of curvature of the substrates. However, upon looking at the interior of the bubbles using this $50X$ microscope objective, we discovered the presence of sizeable pits, as shown in Fig.(3.6). This problem took us somewhat by surprise. We did not expect such significant pits due to the high degree of smoothness reported in Cui et. al [19]. These pits are likely to result in scattering losses when we pass light through it. We believe that these pits are probably due to the heating or cooling process. We are still uncertain as to the definite cause of them. Nonetheless, to proceed with the project, we selected the cavity with the smoothest interior (the one in Fig.(3.6)) as seen in the $50X$ objective and built the cavity using it.
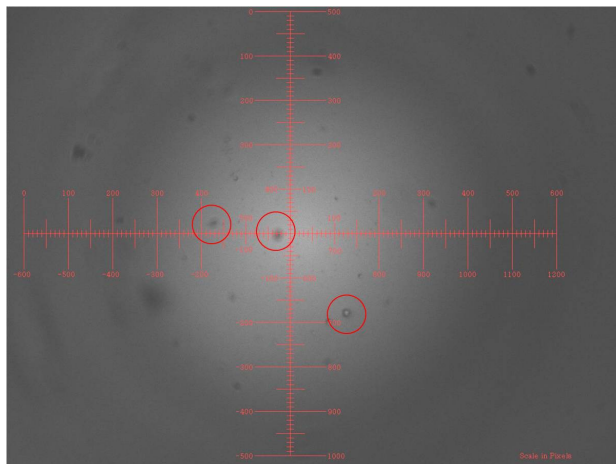
Figure 3.6: **Interior of a bubble after coating under 50X.** This is how the interior of the bubble in the previous figure looked after coating, viewed through a 50X microscope objective. A few pits and blemishes have been circled in red.

3.3 Setup of the Cavity

The cavity was set up as shown in Fig.(3.7). The cavity consists of a plane mirror and the curved micro-mirror of $R_c = 175\mu m$. The plane mirror is epoxy-ed onto a piezo-electric transducer (PZT), which is itself glued onto a macor holder. The glass substrate containing the micro-mirror is epoxy-ed onto an aluminium plate, which is then screwed onto the macor holder to form the complete cavity.

The cavity length was chosen so that the cavity would be mode-matched with our input laser. During operation, a laser of the appropriate beam waist is passed into the cavity. The PZT is connected to a PZT scanner and the potential difference between the two sides of the PZT is varied, causing the length of the PZT to change by small amounts. The transmitted and reflected beams from the cavity are then picked up by a detector connected

to a digital storage oscilloscope, in order to determine the reflection and transmission coefficients of the cavity. As the cavity length changes by small amounts due to the PZT scanner, the cavity resonates in different modes, which will show up as peaks/troughs in the signal of the transmitted/reflected beam signals.
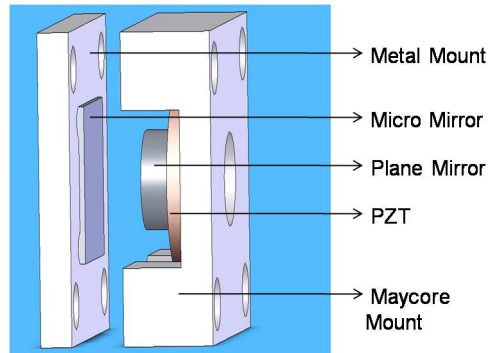

Figure 3.7: **Schematic of Cavity.** The plane mirror is glued on a piezo-electric transducer, which is in turn glued to a macor holder. The length of the cavity, which we found to be $135\mu m$ is given by the sum of the distance between substrates and the depth of the micro-mirror bubble.

The cavity length is given by the sum of the separation between mirrors and the depth of the micro-mirror/dimple. To decide upon the length of the cavity, we made use of Eqs. (2.22) and (2.24).

Making use of Eq. (2.24), we decided that of the lenses easily available on the market, the 11.00mm aspheric lens is the most suitable, as this gives a beam waist that is small enough to allow for wave-front matching between beam and the curved micro-mirror, but not so small that the cavity length would have to be impracticably small. A smaller cavity length would mean higher

34

percentage uncertainty given the same machining apparatus for making the cavity. A very small beam waist would also mean a very large divergence in the beam, which would increase diffraction losses. Making use of this lens, our beam waist was calculated to be $2.75\mu m$ (see section 4.1). To find the right length of the cavity, we then let $R(z) = R_c$ in Eq.(2.22), where R_c is the curvature of our micro-mirror, and solve for z to find a value of $170\mu m$. This gives us the ideal length of the cavity for resonance of $\text{TEM}_{0,0}$ modes. The machining tolerance of our CNC (computer numerical controlled) machine used for making holders is on the order of a few tens of microns, based on the experiences of those who used the machine previously. The depth of our micro-mirror was calculated as $70\mu m$ using simple geometry (this will be shown in section 4.3). This means that we should aim to machine the holders such that the separation between the mirror substrates is $100\mu m$. However, given the limited accuracy of the machine, we programmed to machine to create holders which would give a separation of $70\mu m$ instead. This is because a cavity length exceeding $R_c = 175\mu m$ creates an unstable cavity which does not support any modes at all. We would still be able to see resonance of axial modes even if the cavity length were less than the ideal length of $170\mu m$.

Chapter 4

Measurements

This chapter covers the measurements which were done in the process of building the cavity and the measurements which were done to characterize it. We used a $\text{TEM}_{0,0}$ laser at 780nm for these measurements. Firstly, we describe our measurement of the laser's beam waist, w_0 and the Rayleigh length. As mentioned previously, these were used in deciding upon the cavity length. Following this, we describe a method for accurately determining the radius of curvature of our micro-mirror. we then describe our measurement of the cavity length. Lastly, we present results regarding the transmission and reflection properties of the cavity, and finally the measurement of the finesse of the cavity.

4.1 Determination of Beam Waist and Rayleigh length for mode-matching

As mentioned earlier, we couple light into the cavity using an 11.0mm aspheric lens. In order to have good accuracy in our subsequent measurements, we must determine the beam waist precisely. As mentioned in the previous section, this beam waist was used to decide on the length of the cavity so that the beam is mode-matched to the cavity. Beam waists of a few microns cannot be measured using standard beam profilers. Hence, we needed to set up an imaging system to perform this measurement. We measured the beam waist w_0 using a 50X microscope objective connected to a high resolution camera (Lumenera Infinity Series 3).

Before describing the measurement of the beam waist, I shall first describe the procedure which was done to calculate the resolution of the imaging system. We used a white light source to illuminate the edge of a cycle on a resolution target card as shown in Fig.(4.1).

Figure 4.1: **Resolution Target Cards.**

The pixel data of the resulting image seen through the 50X microscope objective was saved using the camera. The pixel data of an image is the matrix obtained when each pixel in the image is replaced with a number representing the intensity of that pixel. The point spread function(PSF) of the system is a Gaussian function while the function representing the shape of the edge is a step function. The system's resolution may be defined as the standard deviation of its PSF. The net image formed by the contributions from both the step and Gaussian functions is their convolution, given by half multiplied by a complementary error function (*erfc*). The *erfc* is defined as

$$\text{erfc}\,(x) = 1 - \frac{2}{\sqrt{\pi}} \int_0^x \text{e}^{-t^2} \text{dt} \tag{4.1}$$

The standard deviation of the Gaussian function used to compute this erfc in Eq. (4.1), is the standard deviation of the PSF. Hence, we may find the resolution by finding the standard deviation of the Gaussian function in the *erfc*.

The curve given by Eq. (4.2), which is simply half of an *erfc*, was fitted to the pixel data using a least-squares-fit.

$$x_1 \cdot \frac{1}{2}(1 - erf\left(\frac{x - x_2}{\sqrt{2}x_3}\right)) \tag{4.2}$$

where x_1 is the amplitude of the Gaussian used to compute the complementary error function, x_2 is the position offset of the Gaussian's mean value from zero, and x_3 is its standard deviation and x is the position coordinate on our Cartesian axes used for curve-fitting. The result of the fit is shown in Fig.(4.2).
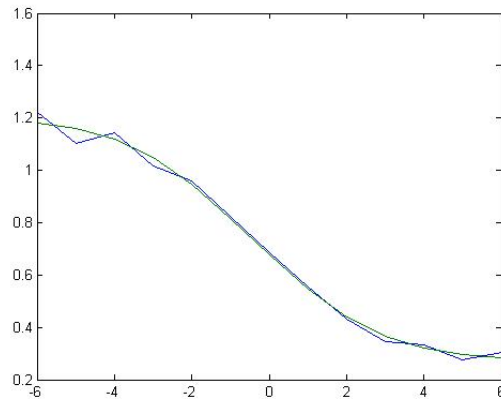
Figure 4.2: **Curve Fit to Pixel Data to Determine Resolution.** The blue line represents the pixel values at the edge of a cycle, while the green line is our curve fit. The standard deviation of the Gaussian is half of the resolution.

The resolution of the camera is given by twice the standard deviation[1]of the Gaussian obtained from the curve fit done in Matlab. This procedure yielded standard deviation of $0.383\mu m$ and thus a resolution value of $0.764 \simeq 0.8\mu m$ for the resolution of our imaging system. The resolution of our imaging system is thus fairly high and will be sufficient for our purpose of imaging beam waists on the order of a few microns.

It is worth noting that the resolution in our imaging system was calculated using a white light source, whereas the laser wavelength we used for subsequent measurements was $780nm$. However, even if the resolution at $780nm$ is twice as large as that which we measured for visible light, the resulting un-

---

[1]It was found using Mathematica that two identical Gaussian functions plotted on the same axes will superpose to form a curve with only a single hump once their respective peaks are separated by 2 standard deviations and below.

certainties in our subsequent measurements can be shown to increase within acceptable limits. This will be done later as the measurements are reported.

The calibration of the camera was also done using these target cards. The result of the calibration was that each pixel represented $0.15 \pm 0.03 \mu m$, where the uncertainty arose from the uncertainty in the length of each line pair on the target card, which was given as $\pm 1 \mu m$.

To image the beam waist of the laser, the imaging system was placed on a translation stage, and moved until the smallest spot size was seen on-screen. This spot size corresponds to the waist of the beam. The image was captured and the pixel data loaded into Matlab once again. The expected intensity profile of the $\text{TEM}_{0,0}$ beam is proportional to the modulus square of the electric field given in Eq. (2.20), with the hermite polynomial terms both set to 1, reflecting that we are using a $\text{TEM}_{0,0}$ beam, and with the substitution $z = 0$, reflecting the situation that we are looking at the cross-section of the beam at its waist. The intensity profile is thus given by

$$I = \text{constant} \cdot \text{e}^{-\frac{2r^2}{w_0^2}} \tag{4.3}$$

It is not important for our purposes to specify the constant terms in the above equation. Hence, the following curve was fitted to the pixel data using a sum-of-least-squares fit.

$$x_1 \cdot \text{e}^{\frac{(x-x_2)^2}{(x_3)^2}} + x_4 \tag{4.4}$$

where x_1 is the amplitude of the intensity profile, x_2 is the offset of the peak

of the profile from the origin, x_3 is the waist of the beam, x_4 accounts for any background offsets to the intensity profile such as stray light sources, and x is the position coordinate on our Cartesian axes used for curve-fitting.

The curve fit is shown in Fig.(4.3). The width of our fitted curve, represented by x_3, is $2.85\mu m$.
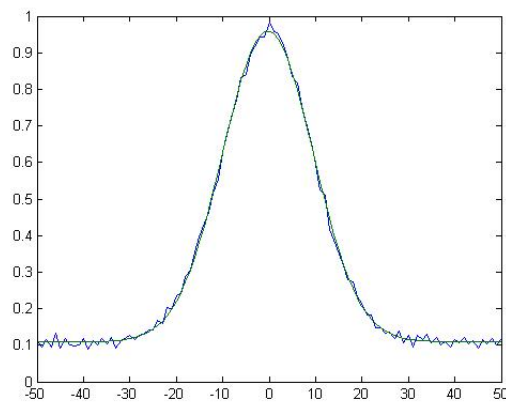

Figure 4.3: **Curve Fit to Pixel Data to Determine Beam Waist.** The blue line represents the pixel values of the spot, while the green line is the curve fit. The standard deviation tells us our beam waist.

Taking the resolution of the camera into account, the beam waist is then given by

$$w_0 = 2 \cdot \sqrt{(\frac{\text{width measured}}{2})^2 - (0.383)^2} = 2.75\mu m \qquad (4.5)$$

The Rayleigh length, z_R, is related to the beam waist via the following formula

41

$$z_R = \frac{\pi w_0^2}{\lambda} = 30.5 \mu m \qquad (4.6)$$

where we use $780nm$ light.

There are two sources of error in this measurement. The uncertainty in this measurement of w_0 due to the resolution of the camera is given by the difference between the waist measurements with and without taking the resolution into account. This works out to $0.1\mu m$. The second source is the calibration of the camera, which contributes an uncertainty of $0.7\mu m$ for this measurement. Taking these uncertainties together, our beam waist measurement is $2.8 \pm 0.8\mu m$. As mentioned earlier, even if the resolution is twice as bad at $780nm$, the difference to w_0 is not severe. If the resolution doubles, the beam waist changes by $0.3\mu m$, which we take to be the uncertainty contribued by resolution. Together with the uncertainty from the calibration process, this gives a total uncertainty of $1\mu m$ for our beam waist measurement. This represents only a 4.8% increase in uncertainty, which means that the uncertainty of the measurement is still acceptable.

The error in z_R is given by the error propagation formula

$$\frac{\delta z_R}{z_R} = 2\frac{w_0}{w_0}$$

which results in uncertainty of $20\mu m$. Hence, $z_R = 30 \pm 20\mu m$. Using the above formula, it can be shown once again that if the resolution is twice as bad, the uncertainty of z_R does not increase very much (it increases by $4\mu m$), though admittedly the uncertainty is rather high for the Rayleigh length of our beam.

4.2 Method for Measuring Radius of Curvature

Before putting the mirrors together in a cavity setup, the radii of curvature (denoted henceforth as R_c) of the the mirrors must be accurately known in order to make the relevant calculations. The R_c of the curved micromirrors were first measured under a microscope 5X objective before they were sent for coating. The R_c were measured by looking at the bubbles through the 5X microscope as they were being polished down. The R_c is taken to be half of the largest diameter seen during the polishing process. The uncertainty of length measurements in the microscope is estimated to be about $10\mu m$, corresponding to the uncertainty of length measurements made on the microscope. This method assumes that the bubble is measured when the it has been ground to its midpoint or near it. In practice, the bubble was not measured in real-time as it was ground down. Instead it was repeatedly ground down by small amounts and measured under the microscope after each grinding interval. The height of glass ground away at each interval was slowly reduced as the bubble was exposed, starting from about $50\mu m$ at each interval when the bubble was first exposed under the microscope, and then going down to as slow as $30\mu m$ per interval as the bubble was further exposed. However, this method should still give a good measurement of the radius of curvature due to the following reason.
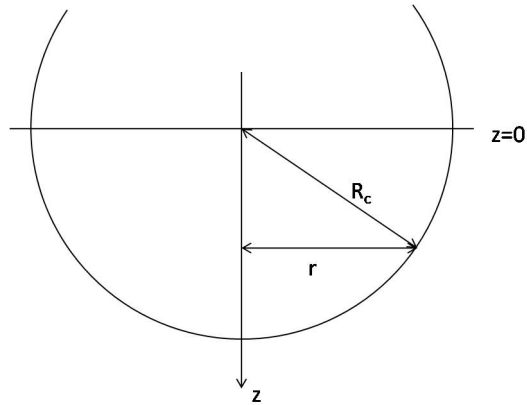
Referring to Fig. (4.4), it is clear that

Figure 4.4: **Diagrammatic Representation of Bubble being Polished.** The z coordinate gives the depth of the bubble, with $z = 0$ defined as the line running through the center of the sphere. R_c is the radius of curvature and r is half of the length seen and measured on the microscope.

$$r = \sqrt{R_c^2 - z^2} \tag{4.7}$$

with $r = R_c$ occuring at $z = 0$ as expected. It is easy to show that the rate of change of r becomes extremely slow near $z = 0$.

$$
\begin{aligned}
\frac{\mathrm{d}r}{\mathrm{d}z} &= -\frac{z}{\sqrt{R_c^2 - z^2}} \\
&\approx -\frac{z}{R_c} \text{ for small } z
\end{aligned}
$$

R_c is typically $150 - 200\mu m$ for our substrates. For small values of z, say $30\mu m$, corresponding to the case where we have polished till very near the halfway point of the bubble, $\frac{\mathrm{d}r}{\mathrm{d}z}$ is on the order of 0.01, which means that the value of r should be very near to that of R_c at this point. Hence, if we take the value of r as our R_c value when we are slightly off from the halfway

point, the resulting discrepancy between the two values is acceptably low. We assumed perfect sphericity of the bubble in this analysis. This assumption should be reasonable due to the high degree of sphericity measured by Cui et. al [19]. Also, we conducted a second measurement to confirm the value of R_c which also supports that the bubble is spherical to within a small margin of error. This measurement will be described shortly.

For the substrate which was used to make the actual cavity, R_c was measured at $175\mu m$ under the microscope. We may verify the above analysis for our case by noting that if we were $30\mu m$ away from the actual halfway point of the spherical bubble when the measurement was made, the actual true R_c is given by $177\mu m$, which we find using a simple rearrangement of Eq. (4.7).

After the glass substrates were coated, we conducted another measurement of R_c to verify the accuracy of the R_c values measured using the microscope. This measurement also allows us to verify the sphericity of the bubble. The procedure is represented diagrammatically in Fig.(4.5) and is described as follows.

The radius of curvature, $R(z)$, of a TEM$_{0,0}$ Gaussian beam varies according to Eq. (2.22), which is re-written here for easy reference.

$$R(z) = z(1 + (\frac{z_R}{z})^2) \tag{4.8}$$

where $R(z)$ is the curvature of the beam at the point z along the axis of propagation, $z = 0$ is defined as the position of the beam's waist, and z_R
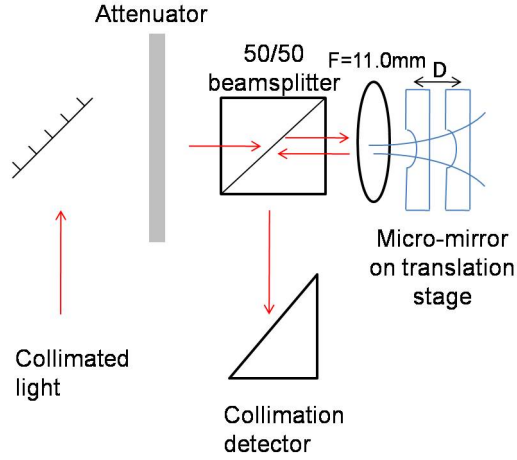
Figure 4.5: **Setup for determining** R_c**.** The position of the micro-mirror is varied by means of a translation stage. As the substrate is moved along the direction of laser propagation, the surface of the curved micro-mirror matches the laser wave front at two positions, causing a collimated beam to be detected. The difference between these two positions, D, can be used to find R_c via Eq.(4.10)

refers to the Rayleigh length of the beam. The radius of curvature of the beam, $R(z)$ will be equal to the R_c of the micro-mirror at two points. (This is obvious from the fact that there are two solutions for z when we solve the quadratic equation $R(z) = R_c$.) The difference between the 2 z solutions, denoted by D, is simply the difference between the 2 roots of the quadratic equation, given by

$$D = \sqrt{R_c^2 - 4z_R^2} \qquad (4.9)$$

We find D by starting with the micro-mirror near the lens, and then slowly increasing its distance from the lens. When we first observe a collimated beam being reflected to the detector, we record the reading on the translation

stage's micrometer. Note that this reflection occurs because the interior of the bubble has been coated. We then continue moving the substrate away from the lens till we detect a collimated beam at the detector once again and record the translation stage micrometer reading. The difference between these two readings is equal to D. The R_c can then be found by solving for R_c in the previous equation. Hence,

$$R_c = \sqrt{D^2 + 4z_R^2} \tag{4.10}$$

where we already know the Rayleigh length z_R from our earlier measurement. The uncertainty of this measurement is derived as follows.

Starting from Eq. (4.10), and making use of typical error propagation formulae, we get

$$
\begin{aligned}
\frac{\delta R_c}{R_c} &= \frac{1}{2}\frac{\delta\left(D^2 + 4z_R^2\right)}{D^2 + 4z_R^2} \\
&= \frac{1}{2}\frac{\sqrt{\left(\delta D^2\right)^2 + \left(4\delta z_R^2\right)^2}}{D^2 + 4z_R^2}
\end{aligned}
\tag{4.11}
$$

with

$$
\begin{aligned}
\frac{\delta D^2}{D^2} &= 2\frac{\delta D}{D} \\
\frac{\delta z_R^2}{z_R^2} &= 2\frac{\delta z_R}{z_R} \\
\frac{\delta z_R}{z_R} &= 2\frac{\delta w_0}{w_0}
\end{aligned}
\tag{4.12}
$$

where the last equation is due to the fact that z_R is related to the beam waist w_0 via Eq. (2.23). Given these equations, once we know the uncertainties of D and w_0, we can compute the percentage uncertainty using Eq. (4.12). δD is simply the uncertainty of length measurements made on the micrometer screw gauge of the translation stage, which is $10\mu m$. δw_0 was found to be $0.8\mu m$ in the previous section. Making use of these values and the equations above, we arrive at a percentage uncertainty of 8% for the R_c measurements done using this method.

Once again, if the resolution is twice as large as what we measured, the percentage uncertainty is found to increase only to 10%, which is still acceptable.

The above procedure was not carried out using the actual substrate due to a concern that this may damage the coating, but was carried out using another substrate with a curvature measured at $185\mu m$ using the optical microscope. The resulting reading obtained was $187\mu m$. Hence, the readings done on the microscope and using the method just described are consistent within their error margins. The fact that these two measurements agree with each other supports the conclusion that the bubbles indeed have a high degree of sphericity. (One may have suspected that the cross-section of the bubble looks circular, but the base of the bubble is not indeed spherical. This measurement shows that this is not so.)

In conclusion for this section, we are confident that the R_c measurement of our chosen substrate of $R_c = 175\mu m$ is accurate to within 10% or $17.5\mu m$.

4.3 Measurement of Cavity Length

The total length of the cavity, L_{cav}, is given by the sum of the separation distance between the mirrors, S and the depth of the micro-mirror, D_h, as shown in Fig. (4.6).

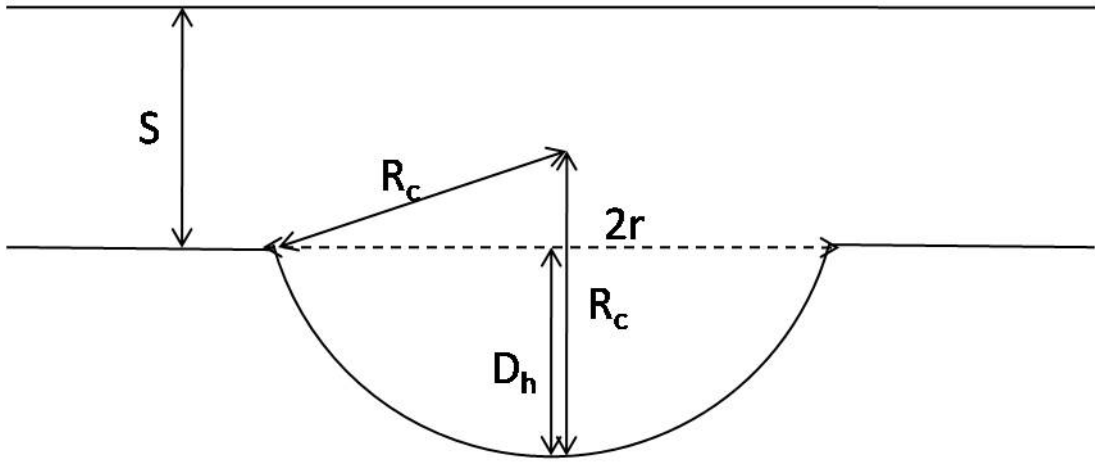Figure 4.6: **Sidelong View of Cavity** The length of the cavity is clearly given by the sum of mirror separation S and micro-mirror/dimple depth D_h.

The depth of the micro-mirror is easily worked out using the formula

$$D_h = R_c - \sqrt{R_c^2 - r^2} \tag{4.13}$$

$2r$ is the diameter of the circle seen under the microscope when the bubble was ground to its final depth. This was measured on the the same optical microscope used previously and was found to be $280 \pm 10\mu m$. This gives D_h a value of $70\mu m$.

The measurement of the separation yielded $S = 65 \pm 10\mu m$.

Hence, we obtain

$$L_{cav} = D_h + S = 135\mu m \tag{4.14}$$

The uncertainty of this measurement is given by

$$\delta L_{cav} = \sqrt{(\delta D_h)^2 + (\delta S)^2} \tag{4.15}$$

The uncertainty δD_h is obtained as follows.

$$
\begin{aligned}
\delta D &= \sqrt{(\delta R_c)^2 + \left(\delta\sqrt{R_c^2 - r^2}\right)^2} \\
\frac{\delta\left(\sqrt{R_c^2 - r^2}\right)}{\sqrt{R_c^2 - r^2}} &= \frac{1}{2}\frac{\delta\left(R_c^2 - r^2\right)}{R_c^2 - r^2} \\
\frac{\delta R_c^2}{R_c^2} &= 2\frac{\delta R_c}{R_c} \\
\frac{\delta r^2}{r^2} &= 2\frac{\delta r}{r}
\end{aligned}
$$

We need only substitute into the above equations the values of $\delta R_c = 10\mu m$, $\delta r = 5\mu m$ corresponding to uncertainty for measurements done on the microscope, to obtain $\delta D_h = 18\mu m$. We substitute δD_h and δS into Eq. (4.15) to obtain $\delta L_{cav} = 20\mu m$.

4.4 Transmission and Reflection Properties of Cavity

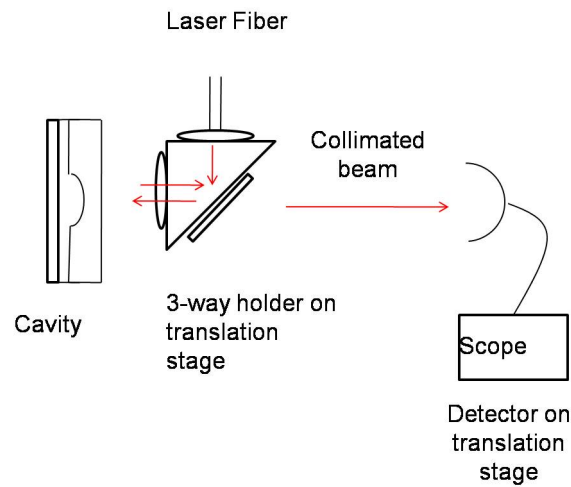We measured the reflection of the cavity on-resonance by using the following method, displayed in Fig.(4.7).

Figure 4.7: **Setup for measuring reflection of cavity on resonance.** The three-way holder contains two 11.00mm aspheric lenses (ovals) and one uncoated window (rectangle). The holder's position is varied on a translation stage such that the beam curvature matches that of the curved micro-mirror. This causes a collimated beam to be reflected from the cavity back into the detector. Since the PZT is sweeping, we will also observe troughs in our reflection signal.

Light from the fiber is collimated by an 11.00mm aspheric lens, reflected by an uncoated window and re-focused onto the cavity. The position of the lenses is varied until the curvature of the beam matches that of the

micro-mirror. (The alignment is facilitated by placing a television camera behind the cavity.) When the wave front coincides with the surface of the micro-mirror, a collimated beam is reflected back into the detector. Hence, we know that the beam is aligned with the cavity when we see most of the laser's input power to the cavity being reflected into and read by our detector. As mentioned in Chapter 2, the PZT is connected to a PZT scanner which varies the potential difference across the PZT over a range of $1000V$ at a rate of $110Hz$. The PZT length changes by $400nm$ per 1000V applied across it. The plane mirror is expected to oscillate over one free-spectral range of the cavity given by $390nm$, which is half the wavelength of light used. We expected to be able to capture the privileged mode of the cavity in our scope as we scan the PZT over its full scan range. However, we found that the PZT did not appear to cover one full free spectral range when a sweep over $1000V$ was applied. We believe that this is due to how the PZT is placed within the cavity- it is possible that the PZT is experiencing friction with the cavity holder.

After aligning the beam with the cavity and switching on the PZT scanner, we observed troughs in the reflected signal as shown in Fig.(4.10). Upon trying my best to align the cavity, and also lowering the sweep range of the PZT to isolate a single mode, the signal in Fig.(4.9) was obtained. If we approximate that the signal in Fig.(4.9) at the horizontal segments represent 100% reflection of light from the cavity, then the reflection coefficient at resonance can be found by taking dividing the magnitude of the signal at the lowest point by that at the straight line region. This procedure yields a reflection coefficient of 92.2%. Clearly, the drop in the signal is far from

the complete disappearance of the reflected signal which is expected during resonance of an ideal cavity. This is due to the high absorption coefficient of the coatings supplied to us and also presumably due to the pits in the curved micro-mirror and/or differences in the coatings of the two mirrors due to uneven deposition of the coating on the curved surface of the micro-mirror. Due to the extremely low transmission on the coatings supplied to us, it is not possible for us to accurately quantify the scattering losses. This is explained in detail as follows.
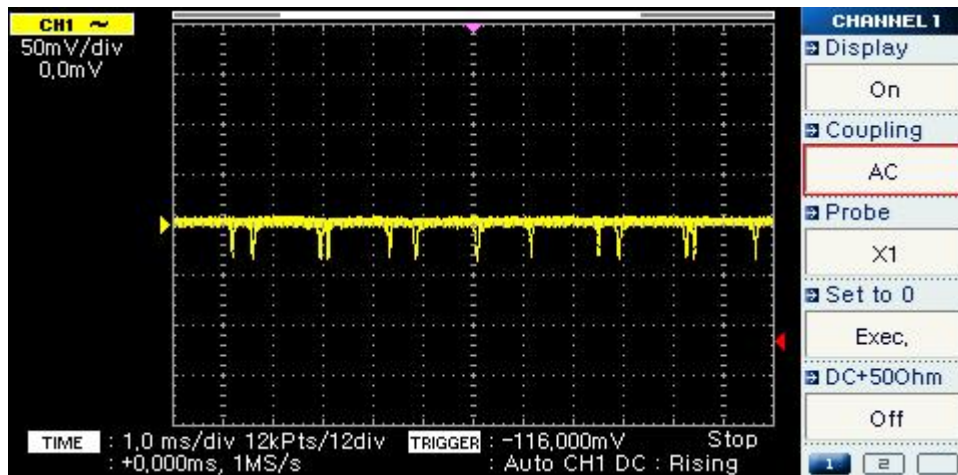

Figure 4.8: **Reflected signal before fine-tuning alignment.** The cavity undergoes resonance at many different modes as the PZT sweeps over 1000V. The scope is set to display alternating current signals.

The company provided us with their measurements of the transmission coefficients for their coatings. This was given as 0.02% or $2.0 * 10^{-4}$ at $780nm$. (Note that this measurement was made using a plane mirror and not our
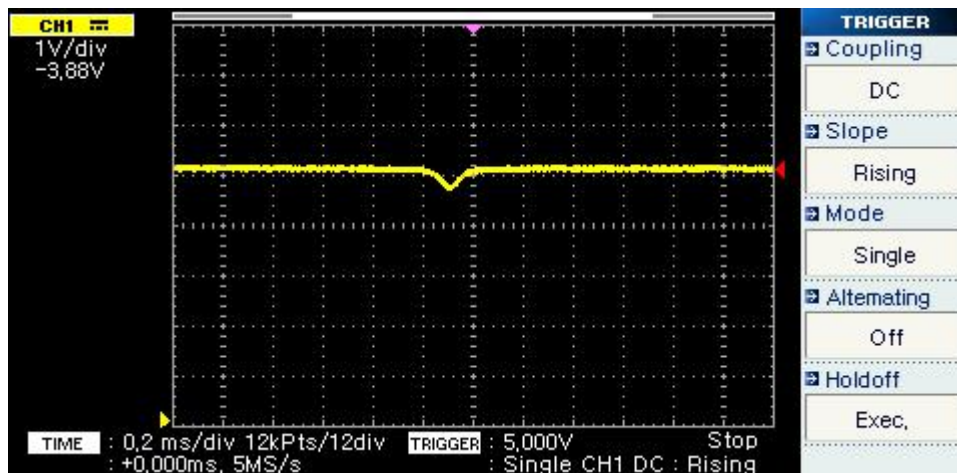
Figure 4.9: **Reflected signal after fine-tuning alignment.** The cavity undergoes resonance at only a single mode. The scope is set to display direct current signals. It is obvious that the reflected signal decreases by only a small fraction of the total signal upon resonance.

custom-made curved micro-mirror.) This was far off from the specifications which we had requested from them. We had requested reflection coefficients of $99.25 - 99.50\%$ or $0.9925 - 0.9950$ with transmission coefficients of $\mathbf{0.25 - 0.5}\%$ at $780nm$. In other words, they provided us with percentage transmission that was an order of magnitude lower than what we wanted. We cannot be sure what the reflection coefficients on the individual mirrors were. The company was able to provide us only with transmission data. We did not measure the refection coefficients ourselves for the following reason. A measurement of reflection coefficient could presumably be made by bouncing light off the mirror, measuring the reflected power and comparing this with the incident power of the light. However, we would not be able to differentiate with reasonable confidence the difference between say 99.25% and 99.5% of the incident power being reflected back into our detector. We

proceed instead by assuming reasonable values for the reflection coefficients in order to make sense of the data in Fig. (4.9).

If we assume that they provided us with the requested reflection coefficients on both coatings, then by Eq. (2.1), we obtain loss coefficients of $0.48-0.73\%$ for the coatings. This is in the scenario where there are no further losses, unlike the case for the micro-mirror surface, where further losses are expected due to scattering from the pits on it. The reflection coefficient of the cavity is given by Eq. (2.8). Making use of this equation and the quantities just mentioned, we obtain an expected reflection coefficient of $91.7-94.0\%$ on resonance. Our approximate measurement of the reflection coefficient of the cavity being about 92.2% during resonance falls within this range. Hence, it is not possible to say conclusively what the effect of the scattering losses or mismatch of the mirror coatings might have been.

We tried also to measure the power transmitted through the cavity by placing another $11.00mm$ aspheric lens and a detector after the cavity in Fig.(4.7). We were able to see the transmitted beam on a screen using a small television camera, but were unable to measure any signal on the detector, even while working with the lights switched off. The reason for this is that given the reflectivity and absorption coefficients of the mirrors supplied to us, the expected transmission is already forbiddingly small even before considering further losses through scattering and cavity mismatch. Hence, in the presence of such effects, the transmission becomes even smaller and beyond the ability of our detectors to measure accurately. This is explained in more detail as follows.

The transmission of the cavity is given by Eq. (2.7). Subsitituting the same values for reflectivities and absorptivities as before, we obtain an expected transmission of $0.07 - 0.1\%$. Again, this is without considering possible scattering losses from the pits or mismatch of coatings. Since we are shining in power of about $100\mu W$, we can only hope to detect transmitted power of about $100nW$, a forbiddingly small amount. Hence, the presence of any further loss mechanisms is likely to push down the transmitted power to an amount which is beyond our ability to measure. This is what we believe happened in our case- further losses such as the mismatch of the reflection coefficients and/or scattering losses from the pits are present. The transmitted power must have been smaller than the ambient background lighting in the lab even with the lights switched off, resulting in our inability to read any change in the detector signal caused by the transmitted light. Since our camera was able to 'see' the transmitted light, we *could* have calibrated a camera to measure the transmitted power. However, given the very low power being transmitted, any inferences made from such a measurement would remain inconclusive, as any small random errors, such as fluctuations in background lights, would have a magnitude comparable to that of the measurement itself.

To conclude this discussion on the transmission of the cavity, the transmission through the cavity is negligibly small, below 0.1%, even on resonance. This is due to the quality of the coatings supplied to us, and also due to the likely presence of significant scattering losses and possibly cavity mismatch as well. We cannot quantify these losses because we are unable to measure the transmitted light. We did not venture toward using higher incident beam powers because this was likely to damage the coatings- if the coatings were

damaged, the reflectivities would change and we would not have a clear picture of what was happening.

4.5 Observation of Cavity Modes

We were able to observe some reasonably well-defined modes within the cavity itself by imaging the surface of the flat mirror within the cavity using the imaging system described previously- a $50X$ microscope objective connected to a high resolution camera. During this procedure, the sweep of the PZT scanner was set to zero so that the potential difference across the PZT was no longer oscillating. The potential difference was then varied manually by changing the offset on the scanner. We were able to observe the modes of the cavity as shown below.
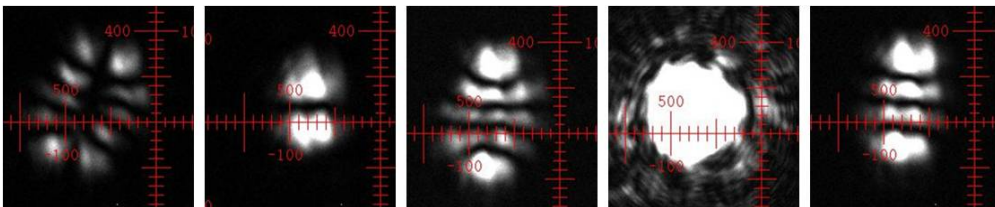

Figure 4.10: **Modes were observed as the PZT voltage was manually scanned.** From left to right, the above modes were seen as the voltage was at 170, 458, 612, 800 and 968 V respectively. These correspond to $TEM_{4,1}$,$TEM_{1,1}$,$TEM_{4,0}$,$TEM_{0,0}$ and $TEM_{3,0}$ modes.

4.6 Finesse Measurement of Cavity

We measured the finesse of the cavity by the following method. The cavity was set up as in Fig. (4.7). An electro-optic modulator was used to place troughs (sidebands) at a known distance in frequency space on either side of the single trough seen in Fig.(4.9), thus generating the signal seen in Fig.(4.11). The distance between the central trough and either sideband corresponds to a frequency difference of 4.6GHz. This gives us a frequency scale which may be used to determine the linewidth and hence the finesse of the cavity. A curve-fit was done in Matlab with the signal seen in Fig.(4.11). The data was fitted to the sum of three Lorentzians. The data is well described by the three Lorentzians as shown in Fig.(4.12). The curve-fitting procedure yields a value for the linewidth of the central Lorentzian, which can be translated into the linewidth of the cavity using the scale established by the sidebands- the distance between the central trough and each sideband corresponds to 4.6GHz, so we can easily find the frequency corresponding to the width of the central Lorentzian. This procedure gives us a value of $1.44GHz$ for the cavity linewidth. Making use of $L_{cav} = 135\mu m$ and Eq. (2.15), we obtain a finesse of 766.

The uncertainty in this reading is due dominantly to the uncertainty in the cavity length L_{cav}. Hence, the percentage uncertainty in this finesse reading may be considered equal to that of the L_{cav} measurement. The uncertainty of the finesse is thus given by
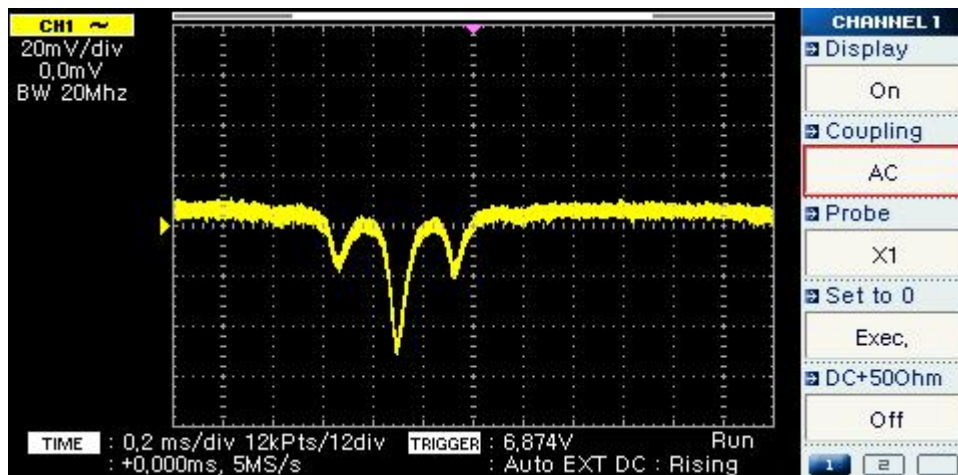
Figure 4.11: **Reflected signal with EOM.** The central trough is the dip in reflected power due to resonance. The two sidebands are each 4.6GHz from the central trough.
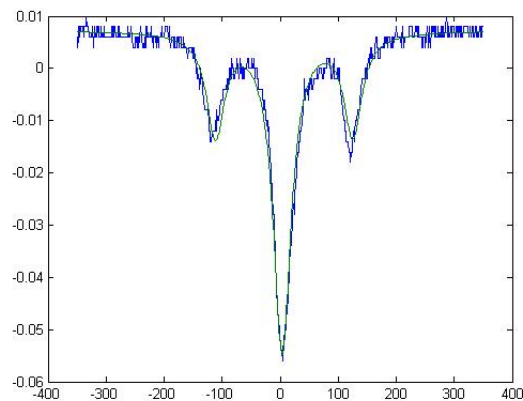

Figure 4.12: **Curve fit of reflected signal to three Lorentzians.** The green line is the curve fit while the blue line is the actual data. The fit looks reasonably good.

$$\delta F = \frac{\delta L_{cav}}{L_{cav}} F = 100 \tag{4.16}$$

Hence, the finesse may be taken to be $F = 800 \pm 100$.

Chapter 5

Discussion and Conclusion

We have done the work of developing and characterizing a micro-cavity. This work has served as a trial run of sorts for the fabrication method described in [19] in which we have obtained various pieces of information which will be useful in the making of micro-cavities which will actually be used for applications such as atom chips or entanglement distribution. This includes discovering the issue of pits being present inside the micro-mirror. Unfortunately, we were unable to quantify the effects of these pits due to the quality of the coatings supplied to us. Our measurements in Section 4.2 suggest that the bubbles indeed possess a high level of sphericity, which makes this method seem promising. We measured the finesse of the cavity as 800.

Now that we have tried making the first microcavity, the next step would be to address the issues which we discovered. These include the problem of pits inside the micro-mirror. One solution to this may be to use an etching to smoothen the interior of the micro-mirror bubble. It might be possible that

Cui et al did not encounter any problem with the pits since they used a very tightly focused laser beam with waist of about $1.0\mu m$. The next step after devising solutions to these issues would be to obtain high quality coatings with high-reflectivity and essentially zero absorption. If these coatings are successfully deposited on the mirror surfaces of the half-symmetric cavity, the requirements for strong coupling will certainly be reachable using such a cavity.

Bibliography

[1] H. J. Kimble, Physica Scripta. **T76**, 127-137 (1998).

[2] C. J. Hood, T. Lynn, M. Chapman, and H. J. Kimble, Phys. Rev. Lett. **80**, 4157 (1998).

[3] H. Mabuchi, Q. A. Turchette, M. S. Chapman, and H.J. Kimble, Optics Lett. **21**, 1393 (1996).

[4] T.W.H Pinkse, T. Fischer, P. Maunz., and G. Rempe, Nature, **404**, 365 (2000).

[5] C.J. Hood, T. W. Lynn, A. C Doherty, A. S. Parkins, H.J. Kimble, Science **287**, 1447 (2000).

[6] M. Trupke, E.A. Hinds, S. Erikkson, E.A. Curtis, Z. Maktadir, E. Kukharenka, M. Kraft, Appl. Phys. Lett., **87**, 211106 (2005).

[7] T.P. Purdy, D.M. Stamper-Kurn, Appl. Phys. B, **90**, 401 (2008).

[8] I. Teper, Y. J Lin, V. Vuletic, Phys. Rev. Lett. **97**, 023002 (2006).

[9] E. A. Hinds, I. G. Hughes, J. of Physics D: Appl. Phys., **32**, R119 (1999).

[10] J. M. Raimond, M. Brune, S. Haroche, Rev. of Mod. Phys., **73**, 565 (2001).

[11] Tatjana Wilk, S. C. Webster, A. Kuhn, G. Rempe, Science, **317**, 488 (2007).

[12] J. Mckeever, A. Boca, A. D. Boozer, R. Miller, J. R. Buck, A. Kuzmich, H. J. Kimble, Science, **303**, 1992 (2004).

[13] P. Maunz, T. Puppe, I. Schuster, N. Syassen, P. W. H. Pinkse, G. Rempe, Nature, **428**, 50 (2004).

[14] S. J. van Enk, J. Mckeever, H.J. Kimble, J. Ye, Phys. Rev. A, **64**, 013407 (2001).

[15] A.C Doherty, T. W. Lynn, C. J. Hood, H. J. Kimble, Phys. Rev. A, **63**, 013401 (2000).

[16] J. T. Verdeyen, *Laser Electronics*, Prentice Hall (1989)

[17] Mark Fox, *Quantum Optics: An Introduction*, Oxford University Press (2006).

[18] R. J. Thompson, G. Rempe, H. J. Kimble, Phys. Rev. Lett., **68**, 1132 (1992).

[19] Guoqiang Cui, J. M. Hannigan, R. Loeckenhoff, F. M. Matinaga, M. G. Raymer, S. Bhongale, M. Holland, S. Mosor, S. Chatterjee, H. M. Gibbs, G. Khitrova, Optics Express **14**, 2289 (2006).